Orientation-dependent properties of epitaxially strained perovskite oxide thin films: Insights from first-principles calculations

Thomas Angsten,* Lane W. Martin,† and Mark Asta‡
Department of Materials Science and Engineering, University of California, Berkeley, California 94720, USA
and Materials Sciences Division, Lawrence Berkeley National Laboratory, Berkeley, California 94720, USA
(Received 9 February 2017; revised manuscript received 4 May 2017; published 30 May 2017)

The structural properties, energetics, and polarizations of perovskite-based thin-film oxide systems are computed as a function of biaxial strain state and epitaxial orientation, employing an automated computational workflow based on density functional theory. A total of 14 compositions are considered, of the form ABO_3, with A = Ba, K, Na, Pb, and Sr and B = Hf, Sn, Ti, Zr, Nb, Ta, and V site cations chosen to yield tolerance factors with values ranging between 0.95 and 1.1. Three biaxial strain states corresponding to epitaxial growth of (100)-, (110)-, and (111)-oriented films are considered, with misfit strains ranging between −4% to 4%. Results are presented for the series of perovskite-derived phases, and their corresponding symmetries, which are energetically favorable as a function of misfit strain, along with their corresponding equilibrium atomic positions, lattice parameters, and electric polarizations. The results demonstrate robust trends of in-plane polarization enhancement under tensile strain for all epitaxial orientations, and out-of-plane polarization enhancement with compression for the (100)- and (110)-oriented films. Strains corresponding to the (111)-growth orientation lead to a wider variety of out-of-plane polarization behavior, with $BaTiO_3$ showing anomalous diminishing polarization with compression. Epitaxial orientation is shown to have a strong effect on the nature of strain-induced phase transitions, with (100)-oriented systems tending to have smooth, second-order transitions and (110)- and (111)-oriented systems more commonly exhibiting first-order transitions. The significance of this effect for device applications is discussed, and a number of systems are identified as potentially interesting for ferroelectric thin-film applications based on energetic stability and polarization behavior. Analysis of polarization behavior across different orientations reveals distinct groups into which compositions can be organized, some of which have polarization dependencies on misfit strain that have not been reported previously.

DOI: 10.1103/PhysRevB.95.174110

I. INTRODUCTION

The discovery of new functional materials (e.g., ferroelectrics, ferromagnets, and ferroelastics) has periodically led to paradigm shifts in technological applications. For example, the technological value of the ferroelectric effect was not realized until the discovery of $BaTiO_3$, a robust and stable ceramic ferroelectric [1]. This led to a rapid proliferation of new devices that are pervasive in many modern technologies [2]. Subsequent searches for other ferroelectrics focused primarily on tuning composition, leading to the discovery of a number of other useful materials, such as $PbZr_{1-x}Ti_xO_3$ [3]. Despite the impact of discovering next generation functional materials, the search effort has relied extensively on serendipitous discoveries, rather than being based on a systematic exploration over the relevant structural and compositional spaces available.

In recent decades, focus has been placed on the integration of ferroelectric thin films into electronic devices [1]. The constrained dimensions of these films make them amenable to device miniaturization. Furthermore, compared to bulk ceramics or single crystals, ferroelectric thin films offer novel routes to property tuning [4]. One such route is applied strain. Ferroelectrics grown as coherently strained thin films can withstand nonhydrostatic strains of several percent [5]. This biaxial strain is provided by the lattice mismatch between the film and the single-crystal substrate, on which the film is grown. Recent improvements in thin-film growth techniques have enabled the direct exploitation of misfit strain in order to finely tune the properties of oxide films [6]. As one example, Haeni *et al.* demonstrated that $SrTiO_3$, normally a paraelectric at all temperatures, exhibits room-temperature ferroelectricity and dielectric properties that are promising for device applications when epitaxially grown at 1% tensile misfit strain [7]. Another route to property tuning is the control of film orientation [8–11]. By changing the orientation of the substrate, the thin film is subjected to different mechanical boundary conditions that can result in the stabilization of entirely different crystal symmetries [12]. For example, Wu *et al.* showed, using a Landau-Devonshire–based thermodynamic model, that the strain-temperature phase diagram of $BaTiO_3$ exhibits significantly different phases and physical properties when subjected to (100), (110), and (111) epitaxial mechanical boundary conditions [13]. More comprehensive reviews of the observed effects of strain and orientation on the phases and properties of thin films, along with a range of relevant examples, can be found in Refs. [4,5,14,15].

The advent of integrated complex-oxide thin films has created a demand for new materials with properties well suited to the array of potential applications [16]. However, just as with bulk ferroelectrics, the search for improved ferroelectric thin-film materials has relied upon chance discovery or incremental improvement of well-known materials. Furthermore, the majority of experimental thin-film growth has focused on (100)-oriented films of well-known perovskite

*angsten@berkeley.edu
†lwmartin@berkeley.edu
‡mdasta@berkeley.edu

oxides over a small range of strain [4,5,16]. Given the recent experimental work demonstrating the unique properties of coherently strained films grown on (110) and (111) substrates [9–11], as well as the possibility of observing novel phases at large misfit strains [17], it is clear that the search for new ferroelectric thin-film materials would benefit from a systematic exploration of the expanded parameter space associated with these materials. One route to a more thorough exploration is provided by automated first-principles computational approaches.

Automated workflows based on density functional theory methods have been developed and applied in high-throughput searches for new materials, in applications spanning energy, structural, and functional materials (e.g., Refs. [18–22], and references therein). Furthermore, previous theoretical work has developed and applied first-principles methods for determining how the structural and polar properties of perovskite thin films depend on epitaxial strain [23–30]. In these methods, epitaxial constraints are imposed on the in-plane lattice vectors of a bulk periodic crystal, thereby isolating the effect of strain from other factors associated with the substrate/film interface and film surface [15]. The result is a mapping of the minimum energy phase and corresponding polarization as a function of misfit strain.

Despite the existence of a first-principles methodology for modeling ferroelectric thin films, high-throughput approaches based on this methodology have not been systematically applied to aid in their design by screening over a large number of epitaxial systems. Similar to the situation in experimental studies summarized above, the focus of prior theoretical studies has been primarily on a small set of commonly grown perovskites on substrates with square-lattice symmetry, i.e., (100)-growth orientations. Of the first-principles studies that have looked at the effects of epitaxial strain applied under (110)- and (111)-oriented growth, only very commonly studied perovskites, such as $BaTiO_3$ and $PbTiO_3$, have been treated [31–33]. A systematic application of current first-principles computational methods to a wide range of systems would provide a preliminary map of ferroelectric polar properties over the thin-film parameter space, which could prove useful to experimentalists attempting to discover new and improved ferroelectric thin-film materials. This map would ideally screen over a large range of the parameter space, weeding out systems unlikely to have interesting properties, and identifying a subset of systems worth more comprehensive study.

In this work, a first step is taken toward generating such results by applying an automated first-principles computational workflow, based on a methodology similar to that employed by Diéguez *et al.* [30], to study the structure and polarization of nonmagnetic ferroelectric oxide films with perovskite-derived structures. This work extends previous related studies [24–30] by considering an expanded range of compositions and by modeling the effects of epitaxial strain in the (110)- and (111)-oriented films (Secs. III B and III C), in addition to the commonly studied (100)-oriented films. In all, 14 perovskite oxides are considered with epitaxial constraints imposed on the (100), (110), and (111) planes of the cubic perovskite structure. Each of these 42 (14×3) thin-film systems are modeled over an 8% (−4% to 4%) misfit strain range.

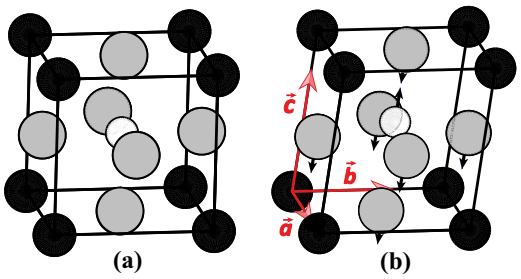

FIG. 1. (a) Ideal cubic perovskite structure with the A cation at the corners (black), the B cation in the body center (white), and the oxygen atoms at the face centers (gray). (b) A possible perovskite-based five-atom unit cell relaxed under (100)-growth orientation constraints. Relative to the cubic structure, this structure has undergone a compressive biaxial misfit strain of $\bar{\eta}$, tensile out-of-plane strain, out-of-plane shear strain, and various (exaggerated) atomic displacements. For (100)-oriented systems, $\|\vec{a}\| = \|\vec{b}\| = a_0(\bar{\eta}+1)$, and $\vec{c}$ is free to relax. This figure was created using VESTA [40].

II. APPROACH

An automated density functional theory (DFT) based workflow has been developed and used to investigate a broad composition-strain-orientation parameter space in order to elucidate fundamental physical trends, as well as search for previously undiscovered polar phases that have the potential to be realized in thin-film growth experiments. To achieve this, the procedure described in Sec. II B is used to predict the minimum energy phases and corresponding structural, energetic, and polarization properties for a number of thin-film systems subjected to various misfit strains and growth orientations. In order to make the search over such a broad parameter space computationally feasible, this workflow employs simplifying assumptions related to the types of crystal structures considered.

Specifically, consideration is given only to structures that can be derived from the primitive cell of the cubic perovskite compound through application of homogeneous strains and atomic displacements, as illustrated in Fig. 1. Thus, this work neglects the consideration of effects such as octahedral rotations and antiferroelectric ordering. These symmetry-lowering effects are expected to suppress polarization rather than enhance it [34], allowing for results in this work to effectively provide upper bounds to the polarization behaviors of the systems considered. Those systems found to be interesting from this initial level of screening can be studied in further detail by applying more rigorous approaches, such as supercell, phonon [35], and molecular dynamics calculations [36], as well as global structure searching algorithms [37–39]. The goal of this effort is to demonstrate a method for such a first level of screening, as well as to identify fundamental trends of thin-film polarization behavior resulting from variations in composition, misfit strain, and orientation, without the additional effects associated with the structural complexities listed above.

A. Selection of compositions

ABO_3 compositions in which the B cations have d^0 electronic configurations in their formal charge state are

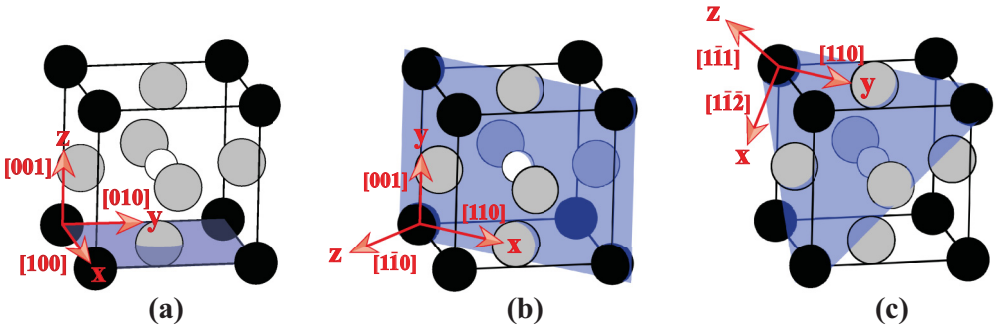

FIG. 2. Orientations of measurement axes for the (a) (100)-, (b) (110)-, and (c) (111)-growth orientations. Cubic crystallographic directions are indicated in square brackets. This figure was created using VESTA [40].

considered. This subset enables a simplification of the workflow due to the absence of spin-polarized states and the need to consider magnetic-ordering degrees of freedom. Furthermore, only compositions having Goldschmidt tolerance factors [41] ranging between 0.95 and 1.1 are considered. The tolerance factor t is defined as follows:

$$t = \frac{R_{A\text{-O}}}{\sqrt{2}R_{B\text{-O}}},$$

where $R_{A\text{-O}}$ and $R_{B\text{-O}}$ are the ideal A-O and B-O perovskite structure bond lengths calculated from the bond valence model [42,43]. For $t > 1$, the B cation is too small for its octahedral cage, favoring a polar distortion. For $t < 1$, octahedral rotations are likely to optimize the A-cation bonding with its 12 neighboring oxygen atoms [44]. For deviations of t far from unity, the perovskite-based structure is likely to become energetically unfavorable relative to other polymorphs. By considering systems with tolerance factors in a constrained range, the chance of a nonperovskite-based polymorph competing with the thin-film phases considered in this work is reduced.

B. Calculation procedure

For each composition considered, the DFT-optimized perfect cubic perovskite structure (space group $Pm\bar{3}m$) is the reference used for reporting misfit strain. To calculate the ground-state phase under particular epitaxial conditions, misfit strain is applied to the appropriate plane [one of (100), (110), or (111)] of the reference cubic structure, and the symmetry is broken by displacing the B cation and oxygen atoms (see next paragraph for details). The positions of all atoms and the lattice vectors are then relaxed until the Hellmann-Feynman forces and out-of-plane stress tensor components converge to magnitudes within 0.001 eV/Å and 0.005 eV/f.u., respectively, where eV/f.u. is per five-atom formula unit. These relaxation criteria give energies converged to within 0.05 meV/f.u., although in almost all cases the forces and stresses are much less than these thresholds, and better convergence is achieved.

In performing the structural relaxations, the mechanical boundary conditions associated with epitaxial growth for a prescribed orientation are enforced. To clearly define these constraints, a convention is used wherein the x, y, and z components of the strain and stress tensors correspond to the choice of axes illustrated in Fig. 2. In terms of these coordinate systems, the mechanical boundary conditions are defined as

$$\epsilon_{xx} = \epsilon_{yy} = \bar{\eta}, \quad \epsilon_{xy} = 0,$$
$$\sigma_{zz} = \sigma_{yz} = \sigma_{xz} = 0,$$

where ϵ and σ are the rotated strain and stress tensors, respectively. Thus, the mechanical boundary conditions are different for each of the three orientations considered in this work. All predicted phases resulting from the structural relaxations correspond to the minimum energy perovskite-based, single-domain, homogeneously strained, periodic structures under epitaxial mechanical boundary conditions and at zero temperature. For all substrate orientations, the misfit strain is calculated as $\bar{\eta} = a/a_0 - 1$, where a_0 is the lattice constant of the cubic reference structure, and a is the necessary lattice constant of a cubic substrate that would impart the given misfit strain. To clarify, an epitaxial lattice constant with a given value a of 4.0 Å refers to the same cubic substrate for the (100)-, (110)-, and (111)-growth orientations, the difference being the preparatory cut of such a substrate crystal.

In the structural relaxations, there are often multiple metastable perovskite-based phases that are very close in energy, especially for misfit strains near a phase transition. The following strategies are employed to ensure the minimum energy perovskite-based phase is found. For each value of misfit strain, at least three of the structural optimizations described above are performed, and the lowest energy of these is taken. For each repetition, the atomic coordinates of the starting structure are randomly seeded with displacements of the atomic positions from the ideal strained perovskite structure having magnitudes up to 0.015 Å for each Cartesian component of each atom position. These displacements generally remove all symmetry for each initial structure, making the space group $P1$. After an initial pass, inspection of the energy curve as a function of strain can still reveal discontinuities where calculations must be rerun. This process of searching for the true ground state at each misfit strain is continued until the energy curve and polarization properties are smooth functions of misfit strain away from first-order phase transitions. For more discussion of the calculation procedure and the details that enable it to be highly automated, see Sec. I of the Supplemental Material [45].

C. Calculation methods

All DFT calculations make use of the Vienna *ab initio* simulation package (VASP) [46–49] version 5.4.1. A conjugate-gradient algorithm is used to relax ionic positions to their ground state. As the standard VASP software package does not allow for arbitrary constraints to be placed on the strain tensor during relaxation, custom modification of the code was required. These modifications set certain components of the stress gradient tensor to zero during conjugate-gradient minimization, allowing for the mechanical boundary constraints (see above) of the three different growth orientations to be simulated.

All calculations use the Ceperley-Alder form of the local density approximation (LDA) exchange-correlation functional as parametrized by Perdew and Zunger [50], and the electron-ion interaction is described using the projector augmented wave method [51,52]. In multiple cases, metastable phases are only a fraction of an meV higher in energy compared to the lowest-energy phase. Consequently, highly converged calculation parameters are required. A 900-eV plane-wave cutoff energy, 6×6×6 Monkhorst-Pack sampling of the Brillouin zone [53], and tetrahedron method with Blöchl corrections [51] are used. The Berry phase approach, as described in the modern theory of polarization [23], is used to calculate the electric polarization vector at each misfit strain. All calculations assume a fixed (vanishing) external electric field corresponding to thin films surrounded by perfectly charge-compensating electrodes. The relevance of this "short-circuit" boundary condition to thin-film growth is discussed in Refs. [54,55].

It should be noted that use of the LDA in this work leads to well-known errors in the calculated lattice constants, which amount to an underestimation of their values on the order of a percent. Previous calculations for perovskite oxide compounds have shown that these errors tend to be systematic across a broad range of chemistries [15,29], and that quantitative values predicted by the LDA are generally in better agreement with experiment relative to those obtained by the generalized gradient approximation [56]. The LDA errors are mentioned explicitly below in those cases where they are relevant in the presentation of the results.

III. RESULTS AND DISCUSSION

Table I lists the chemical formulas, calculated cubic reference lattice constants, and tolerance factors of the 14 compositions considered. The measurement axes used for reporting direction-dependent properties are different for each of the three growth orientations, as illustrated in Fig. 2.

Figure 3 shows, for all compositions and growth orientations considered, the calculated in-plane ($\sqrt{P_x^2 + P_y^2}$) and out-of-plane ($|P_z|$) polarizations of the thin-film systems plotted against the lattice constant of a corresponding cubic substrate. The x axis has been curtailed to the experimentally relevant range of available in-plane lattice constants, and calculated data may extend beyond this range for some systems. It should be noted that the epitaxial lattice constants presented in the horizontal axis of Fig. 3, as well as in Figs. 4–6 below, correspond to misfit-strain values based on the LDA calculations, and are thus expected to be on the order of a percent smaller than true experimental values.

TABLE I. Listing of the 14 compositions considered, along with their calculated cubic lattice constants and Goldschmidt tolerance factors.

Formula	a_0 (Å)	Tolerance factor t
$BaHfO_3$	4.13	1.007
$BaSnO_3$	4.10	1.016
$BaTiO_3$	3.95	1.063
$BaZrO_3$	4.16	1.000
$KNbO_3$	3.96	1.090
$KTaO_3$	3.96	1.085
$NaNbO_3$	3.91	0.972
$NaTaO_3$	3.92	0.968
$NaVO_3$	3.68	1.028
$PbSnO_3$	4.04	0.955
$PbTiO_3$	3.89	0.999
$SrHfO_3$	4.07	0.949
$SrSnO_3$	4.03	0.957
$SrTiO_3$	3.86	1.001

The results plotted in Fig. 3 display several trends, which can be analyzed in relation to previously published observations. For a smaller set of (100)-oriented perovskite oxide compounds, previous works [15,25] have demonstrated trends of out-of-plane and in-plane polarization enhancement under compressive and tensile misfit strain, respectively. The top two plots in Fig. 3 reveal the generality of these two trends across the wider compositional range considered in this work; all (100)-oriented systems show increasing out-of-plane polarization under compression (moving to smaller in-plane lattice parameters) and increasing in-plane polarization under tension (moving to larger in-plane lattice parameters). Interestingly, the trend of in-plane polarization enhancement under tension applies rather generally to all orientations (top left, middle left, and bottom left plots). The out-of-plane polarization for (110)-oriented systems (middle right) is largely enhanced by compression, but less so than for the (100)-oriented systems. The out-of-plane polarization for the (111)-oriented systems shows a variety of behaviors, in addition to enhancement with compression. In the case of only one system, $BaTiO_3$, there is a significantly diminishing out-of-plane polarization with increasing biaxial compression. Many other (111)-oriented systems have large regions of nearly unchanging out-of-plane polarization.

Previous calculations have shown, for bulk ferroelectric perovskites, that c-axis elongation stabilizes polar distortions with atomic displacements in the out-of-plane direction [57]. The above-discussed polarization trends with misfit strain imply that polar distortions can be described in terms of a simple Poisson effect. That is, distortions tend to occur in the general direction of tension, whether it be out of plane or in plane, while distortions tend to be suppressed in compressed directions. In-plane misfit compression causes lattice expansion out of the plane, generally stabilizing out-of-plane polar displacements. Conversely, in-plane misfit tension causes a contraction of the lattice in the out-of-plane direction, disfavoring out-of-plane displacements and stabilizing in-plane polar distortions. Interestingly, this effect

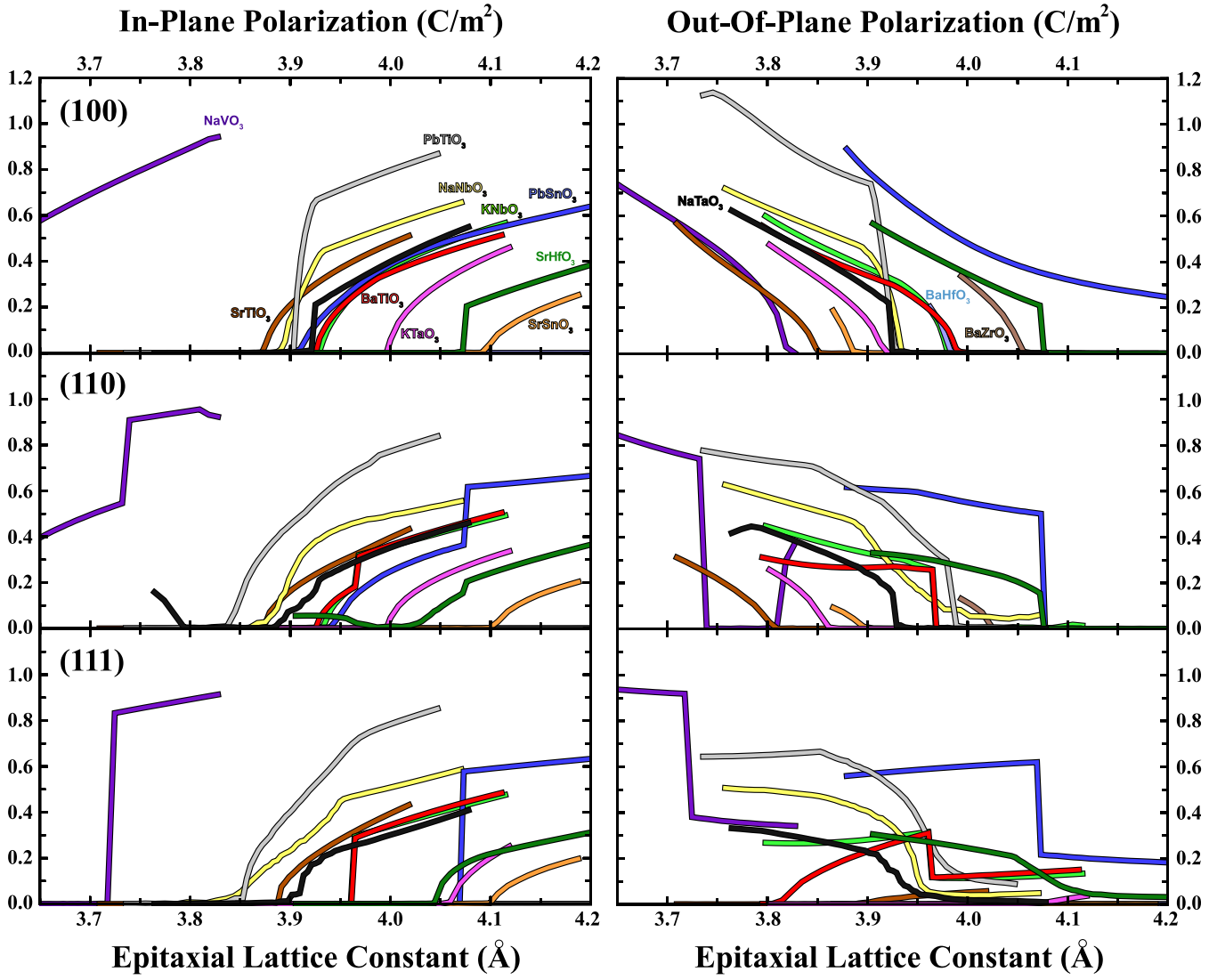

FIG. 3. In-plane (left column) and out-of-plane (right column) polarization magnitudes versus cubic substrate lattice constant for the (100)- (top row), (110)- (middle row), and (111)- (bottom row) oriented systems. The same colors correspond to the same compositions for all six panels.

occurs irrespective of orientation of the applied misfit strain, as shown by the generality of the trend for the (110) and (111) orientations. Furthermore, the anomalously diminishing out-of-plane polarization observed in (111)-oriented $BaTiO_3$ correlates with this system's relatively small out-of-plane lattice elongation when subjected to in-plane compression. This case is discussed in more detail in Sec. III C.

Another trend apparent in Fig. 3 related to the nature of phase transitions between the various orientations. The (100)-oriented systems are largely characterized by smooth curves, featuring second-order transitions between the different phases with changing misfit strain. By contrast, the (110)- and (111)-oriented variants more commonly show first-order transitions, characterized by discontinuities in the polarization (and associated atomic displacements) with changing misfit strain. As sudden switches between polarization states are often intriguing for device applications (e.g., ferroelectric random access memories [15]), film orientation could be a means by which this beneficial behavior is promoted.

Analysis of the full data set produced in this work leads to clear relations between the energetic and polarization properties of various compositions. For a given orientation, there exists a small number of distinct energetic and polarization behaviors by which compositions can be categorized. In fact, each of the 14 compositions can be associated with one of four distinct behavioral groups, and, across different orientations, these groups tend not to change. For example, for the (100)-oriented systems, $BaTiO_3$, $KNbO_3$, $PbSnO_3$, and $NaVO_3$ show similar phase transition behavior and polarization curves. These four compositions furthermore show similar behavior relative to each other for the (110) and (111) orientations, even though the general behavior of this group is significantly different for the three orientations. The organization of these behavioral groups can be clearly visualized in Figs. S1–S3 of the Supplemental Material [45], and an analysis of these groups is given in Sec. III D.

The remainder of this section is divided into three subsections corresponding to highlighted results for the

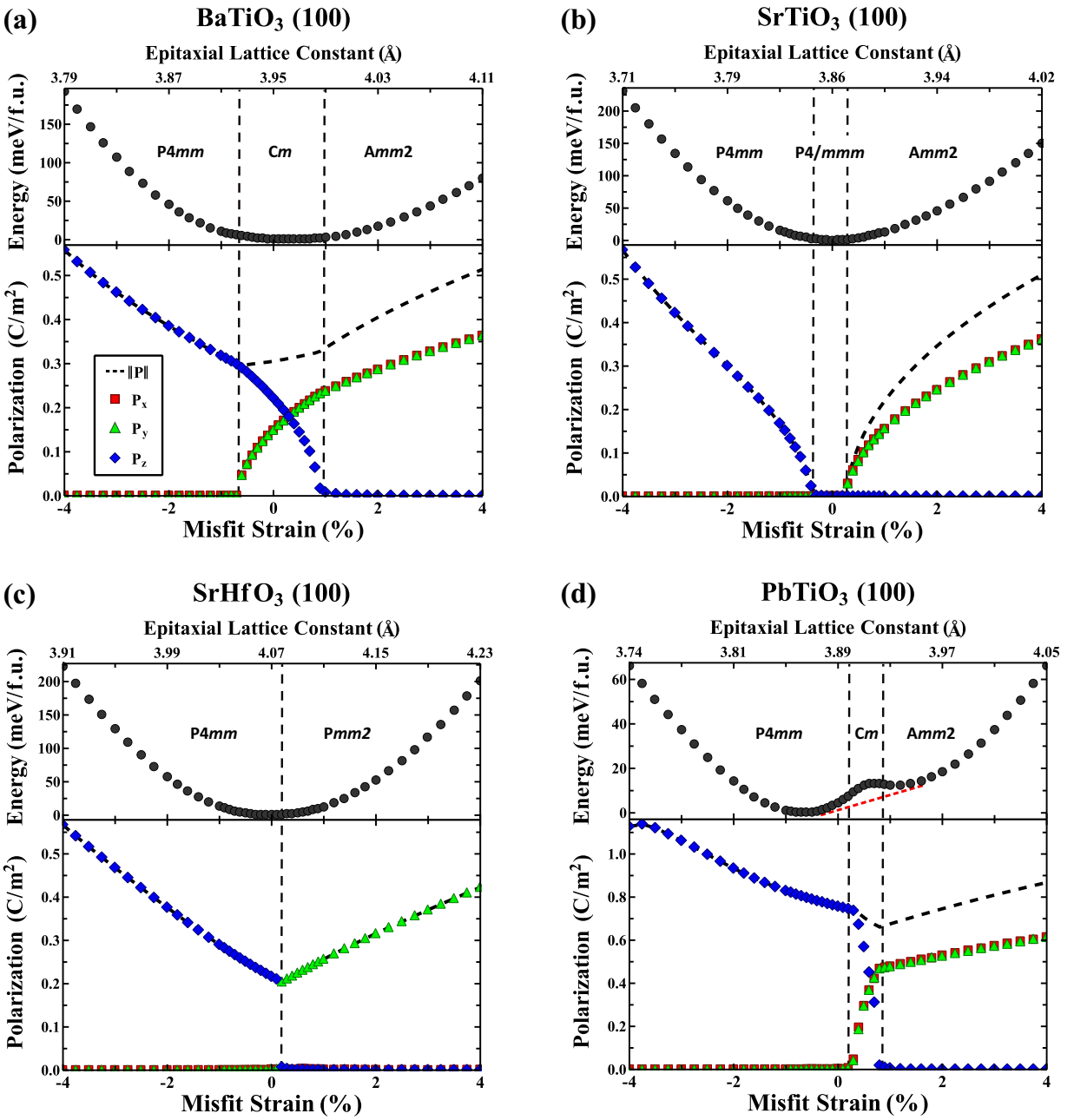

FIG. 4. Energy and polarization as a function of misfit strain for (a) $BaTiO_3$, (b) $SrTiO_3$, (c) $SrHfO_3$, and (d) $PbTiO_3$ on (100). Energies are given in the top panel of each subfigure and are referenced to the corresponding relaxed bulk perovskite-based structure. Regions of phase stability are labeled with the space group symbol and separated by vertical dashed lines. Absolute values of the polarization components have been taken for the purpose of visualization. Polarization vectors are relative to the axes defined in Fig. 2(a).

(100)-, (110)-, and (111)-oriented systems. Only a subset of the data produced in this work is presented in these sections, and, for analogous plots for all of the calculated data, the reader is referred to Figs. S4–S10 in the Supplemental Material [45]. In each subsection, a subset of four representative systems for each orientation is discussed in detail in order to demonstrate the variety of phases and phase-transition behaviors that are observed in the full data set. These four systems are most representative of the four different behavior groups described above.

A. (100)-oriented systems

Table II summarizes the different (100)-oriented phases predicted along with their space group symmetries and a description of the polarization and homogeneous strain state (relative to a cubic reference structure). The (100)-oriented phases predicted in this work are consistent with those found previously in related phenomenological and first-principles computational studies [26,29,58].

Figure 4 presents representative results illustrating the calculated misfit strain dependence of the energy and polarization

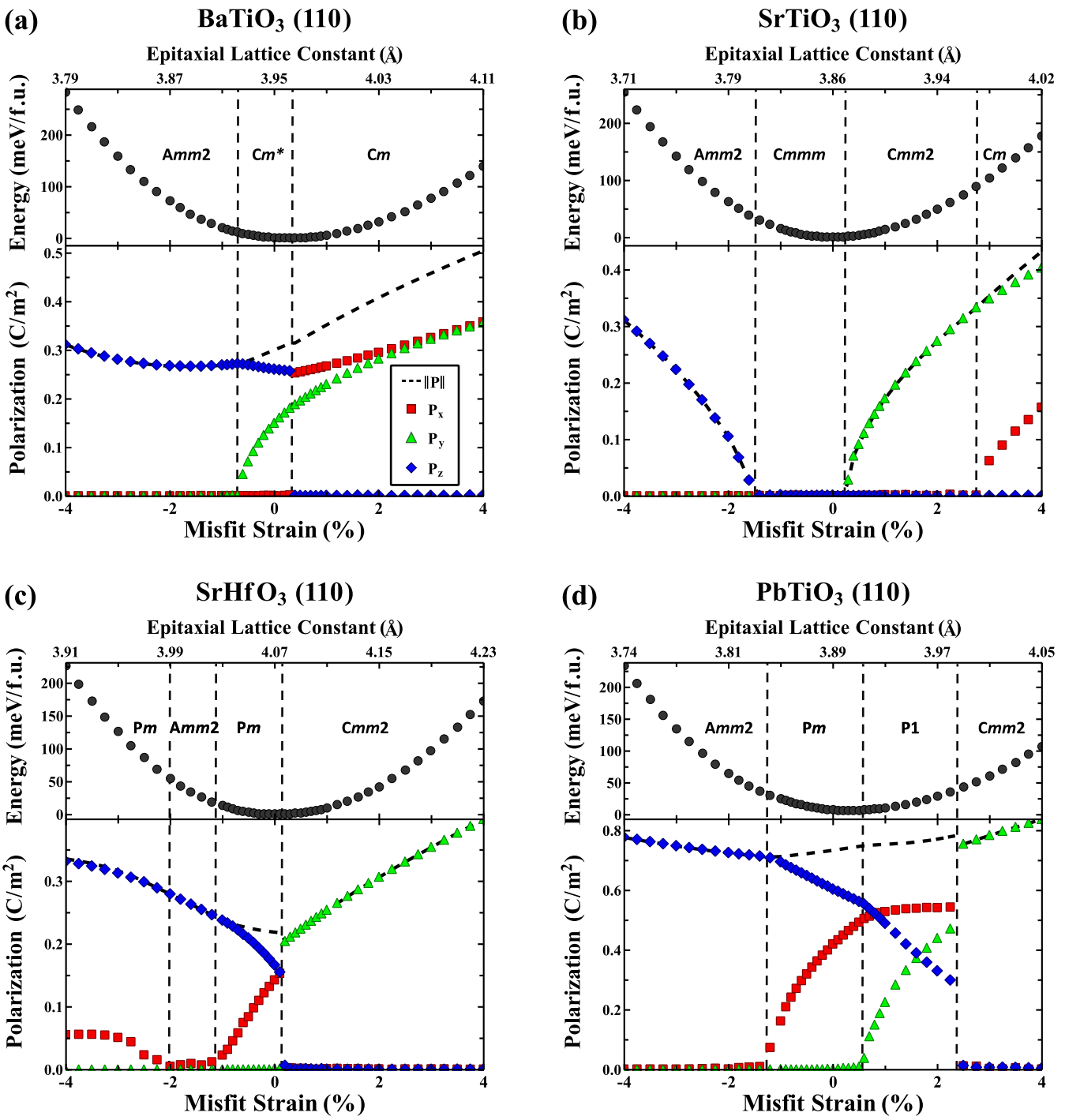

FIG. 5. Energy and polarization as a function of misfit strain for (a) $BaTiO_3$, (b) $SrTiO_3$, (c) $SrHfO_3$, and (d) $PbTiO_3$ on (110). Energies are given in the top panel of each plot and are referenced to the corresponding relaxed bulk perovskite-based structure. Regions of phase stability are labeled with the space group symbol and separated by vertical dashed lines. Absolute values of the polarization components have been taken for the purpose of visualization. Polarization vectors are given relative to the axes defined in Fig. 2(b).

for four different compositions. For each, the energy versus misfit strain is plotted in the upper panel, and the values for the magnitude (dashed line) and out-of-plane (blue diamonds) and in-plane (green triangles and red squares) components of the polarization are plotted in the bottom panel. The horizontal scale on the top of each figure gives the corresponding lattice constant a of a cubic substrate required to produce the given value of misfit: $a = a_0(\bar{\eta} + 1)$, in terms of the reference lattice constant for the given compound a_0. Energies, unless noted otherwise, are referenced to the value corresponding to the equilibrium (likely noncubic) bulk perovskite-based structure for the given composition, and their values can thus be interpreted as representing the strain energy of the epitaxially constrained phase. The more positive the energy, the higher the driving force for strain relaxation, e.g., through formation of misfit dislocations. In the top panel, the space groups for

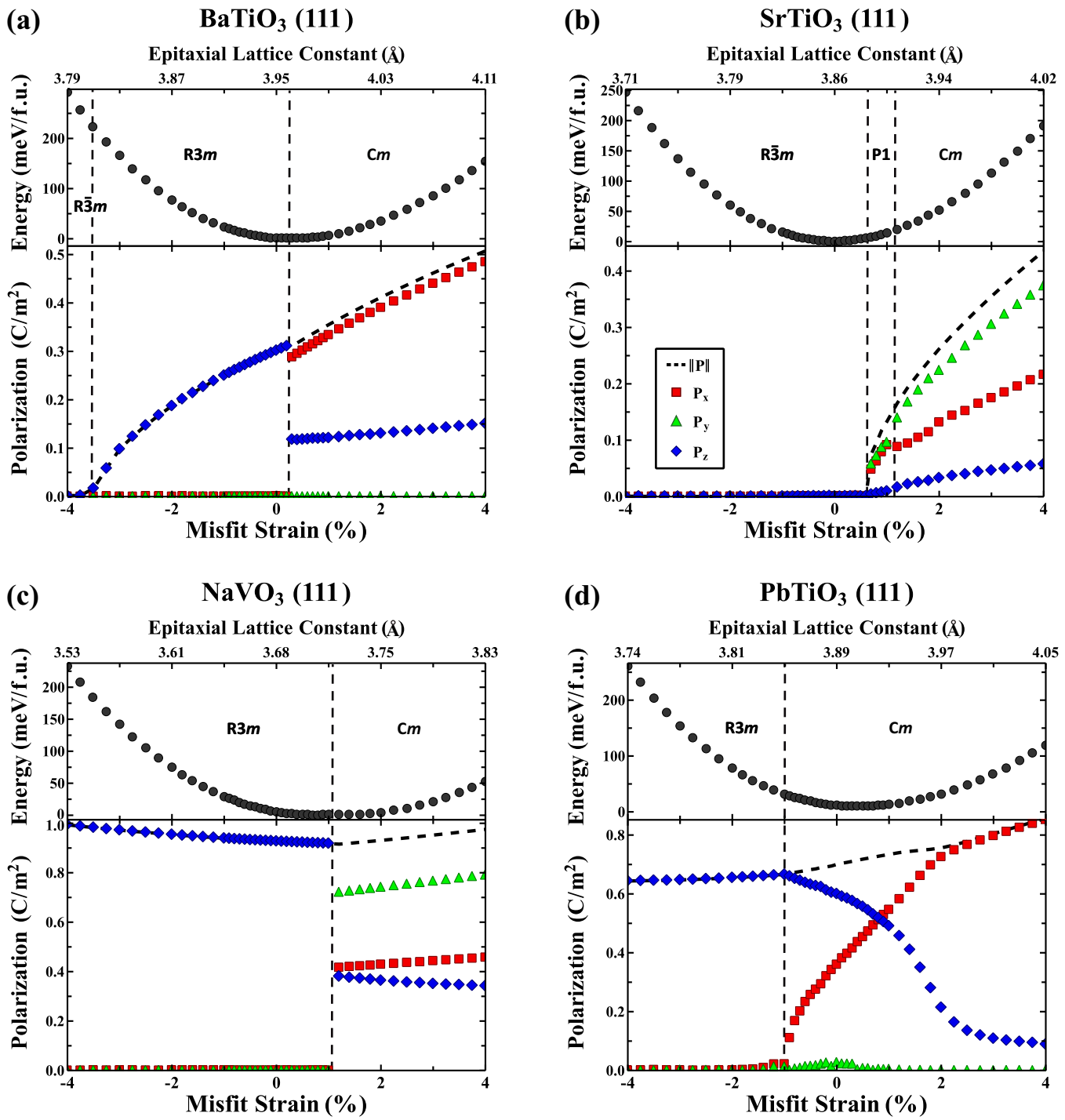

FIG. 6. Energy and polarization as a function of misfit strain for (a) $BaTiO_3$, (b) $SrTiO_3$, (c) $NaVO_3$, and (d) $PbTiO_3$ on (111). Energies are given in the top panel of each plot and are referenced to the corresponding relaxed bulk perovskite-based structure. Regions of phase stability are labeled with the space group symbol and separated by vertical dashed lines. Absolute values of the polarization components have been taken for the purpose of visualization. Polarization vectors are relative to the axes defined in Fig. 2(c).

the epitaxial phase with the lowest energy are indicated, and the dashed vertical lines indicate values of the misfit strain corresponding to phase transitions.

Figure 4(a) presents calculated results for $BaTiO_3$, where the reference bulk structure for the energy calculations is a rhombohedral phase with space group $R3m$, and $a = 3.96$ Å and $\alpha = 89.93^\circ$. Since this energetic reference structure is not cubic, while the structure used to define the reference for misfit strain is, the epitaxial strain with the lowest energy does not occur at $\bar{\eta} = 0$ in Fig. 4(a), but rather at a slightly positive value of $\bar{\eta} = 0.3\%$. Starting from the highest compressive strains and increasing $\bar{\eta}$ to more tensile values, Fig. 4(a) shows that the predicted sequence of phases for $BaTiO_3$ is *c-r-aa* (corresponding to space groups of $P4mm$, Cm, and $Amm2$,

TABLE II. Summary of the observed (100) epitaxial phases, including the commonly used phase name, space group, polarization vector, and Voigt-notated strain tensor. Strains are relative to a cubic $Pm\bar{3}m$ reference structure. p_i and s_i are arbitrary nonzero constants, while $\bar{\eta}$ is the misfit strain. The polarization vector and strain tensor components correspond to the coordinate system shown in Fig. 2(a).

Phase	Space group	(P_x, P_y, P_z)	$(\epsilon_{xx}, \epsilon_{yy}, \epsilon_{zz}, \epsilon_{yz}, \epsilon_{xz}, \epsilon_{xy})$
p	$P4/mmm$ (123)	(0,0,0)	$(\bar{\eta}, \bar{\eta}, s_1, 0, 0, 0)$
c	$P4mm$ (99)	$(0, 0, p_1)$	$(\bar{\eta}, \bar{\eta}, s_1, 0, 0, 0)$
aa	$Amm2$ (38)	$(p_1, p_1, 0)$	$(\bar{\eta}, \bar{\eta}, s_1, 0, 0, 0)$
a	$Pmm2$ (25)	$(p_1, 0, 0)$	$(\bar{\eta}, \bar{\eta}, s_1, 0, 0, 0)$
ac	Pm (6)	$(p_1, 0, p_2)$	$(\bar{\eta}, \bar{\eta}, s_1, s_2, 0, 0)$
r	Cm (8)	(p_1, p_1, p_2)	$(\bar{\eta}, \bar{\eta}, s_1, s_2, s_2, 0)$

respectively, as indicated in Table II). This result is consistent with previous first-principles computed results [26,29]. The predicted misfit strain at which the $c-r$ transition occurs is very close to that of Ref. [26], but the $r-aa$ phase transition is predicted in this work to be at around 1% strain, whereas Ref. [26] predicts this transition to occur at just under 0.7%. This difference is likely attributable to minor variations in calculation parameters, as the energies of the r and aa phases are calculated, in this work, to be within 0.1 meV/f.u. of each other at 0.7% misfit strain.

The calculated polarizations plotted in the lower panel show the onset of an in-plane polarization at the c-r transition, which grows in magnitude with increasing values of $\bar{\eta}$. The out-of-plane polarization decreases in magnitude with increasing tensile misfit strain, vanishing for values of $\bar{\eta}$ beyond the r-aa transition. Three other systems, including $KNbO_3$, $PbSnO_3$, and $NaVO_3$, have phase sequences and qualitative polarization dependencies on misfit strain that are very similar to that shown in Fig. 4(a) for $BaTiO_3$. $KNbO_3$ (Fig. S6 in the Supplemental Material [45]) is the most similar to $BaTiO_3$, having the same phase sequence and nearly the same transition misfit strains, but with a slightly higher average polarization magnitude. $PbSnO_3$ (Fig. S8) and $NaVO_3$ (Fig. S8) also have the same qualitative polarization behavior, but with much broader r (Cm) phase regions. For $PbSnO_3$, this r phase region is so broad that the $Amm2$ phase does not appear in the strain range considered, with the out-of-plane polarization remaining nonzero under the largest tensile strain considered, 4%. Likewise, for $NaVO_3$, the $P4mm$ phase never appears in the range considered, with in-plane polarization remaining nonzero throughout. Such extended r phase regions and gradual phase transitions have not been predicted for (100)-oriented systems in previous studies [26,27,29,30]. Finally, compared to $BaTiO_3$, $PbSnO_3$ and $NaVO_3$ have average polarization magnitudes more than twice as large, around 1 C/m^2 in the case of $NaVO_3$.

Figure 4(b) illustrates a second type of phase behavior observed in the calculations, represented by the specific case of $SrTiO_3$. At zero misfit strain, $SrTiO_3$ is predicted to assume the paraelectric p ($P4/mmm$) phase. Under sufficient compression ($<-0.4\%$), a nonzero out-of-plane polarization develops and the c ($P4mm$) phase is predicted. Under $>0.3\%$ misfit tension, a nonzero in-plane polarization with equal x and y components appears, corresponding to the aa ($Amm2$) phase. The predicted phase order and polarization magnitudes are consistent with Ref. [27], although the paraelectric region in this work is narrower by about 0.5% misfit strain (again, this discrepancy is likely due to differences in calculation parameters). Five other systems exhibit qualitative behavior similar to that illustrated in Fig. 4(b) for $SrTiO_3$, including $KTaO_3$ (Fig. S6), $BaZrO_3$ (Fig. S5), $SrSnO_3$ (Fig. S10), $BaHfO_3$ (Fig. S4), and $BaSnO_3$ (Fig. S4). These systems all have in common a paraelectric p phase region of varying width around 0% misfit strain surrounded by a c phase region to the left and a phase with all in-plane polarization on the right (aa or a). In some cases, the paraelectric phase region is very large, and for $BaSnO_3$, it extends across the entire range considered.

In previous studies of (100)-epitaxially strained systems [26,27,29,30], the phase sequences observed follow the pattern of $c-r, p$, or phase separation $-a$ or aa with smooth, second-order transitions between different phases. With the expanded compositions treated in this work, an additional behavior is predicted having a direct transition from out-of-plane to in-plane polarization. Figure 4(c) illustrates this behavior for the specific case of $SrHfO_3$, for which there is a direct transition from c ($P4mm$) to a ($Pmm2$) at 0.2% misfit strain. To the limit of the resolution of this work's calculations, a direct transition between these two phases occurs without the region of intervening r (Cm) phase found for $BaTiO_3$ and related systems. The other system demonstrating this behavior is $NaTaO_3$ (Fig. S7), which has a c ($P4mm$) to aa ($Amm2$) transition at just above 0% strain. This type of behavior is intriguing from the standpoint of the design of a memory device since the calculations predict that, at around zero misfit strain, the application of a modest in-plane electric field could bias the c phase to transition to a metastable a or aa phase, leading to an extinction of the out-of-plane component of the polarization.

Figure 4(d) shows the polarization and energetic behavior of $PbTiO_3$. Like $BaTiO_3$, the phase sequence is predicted to follow the sequence of $c-r-aa$ with increasing tensile strain. However, due to the presence of concave curvature in the energy, there is a finite range of $\bar{\eta}$ values for which the lowest-energy state is a two-phase mixture of phases having lower and higher values of misfit strain. This strain-induced phase coexistence is similar to phase segregation in alloys of immiscible components, but with strain playing the analog of composition [59]. A visual indicator of this behavior is the existence of a common tangent line that falls below the total energy curve. In the case of $PbTiO_3$, the monodomain r phase is higher in energy than a mixture of c and aa phases between misfit strains of -0.3% and 1.7%, as indicated by the red dashed line in Fig. 4(d). This phase-separation behavior for epitaxially strained $PbTiO_3$ has also been predicted in Ref. [29].

Other (100)-oriented systems predicted to exhibit strain-induced phase separation behavior are $NaNbO_3$ and $NaVO_3$. $NaNbO_3$ has a similar phase ordering to $PbTiO_3$ but with a broader predicted range of strains corresponding to the two-phase state, and less pronounced energetic driving force for phase separation (Fig. S7 in Ref. [45]). $NaVO_3$ is predicted to have a mixture of the r and aa phases between 2% and 4% misfit strain (Fig. S8). The upper bound of this region is

TABLE III. Summary of the observed (110) epitaxial phases, including the space group, polarization vector, and strain tensor given in Voigt notation. Strains are relative to a cubic $Pm\bar{3}m$ reference structure. p_i and s_i are arbitrary nonzero constants, while $\bar{\eta}$ is misfit strain. The polarization vector and strain tensor components correspond to the coordinate system shown in Fig. 2(b).

Space group	(P_x, P_y, P_z)	$(\epsilon_{xx},\epsilon_{yy},\epsilon_{zz},\epsilon_{yz},\epsilon_{xz},\epsilon_{xy})$
$Cmmm$ (65)	(0,0,0)	$(\bar{\eta},\bar{\eta},s_1,0,0,0)$
$Amm2$ (38)[a]	$(0,0,p_1)$	$(\bar{\eta},\bar{\eta},s_1,0,0,0)$
$Cmm2$ (35)	$(0,p_1,0)$	$(\bar{\eta},\bar{\eta},s_1,0,0,0)$
Cm (8)	$(p_1,p_2,0)$	$(\bar{\eta},\bar{\eta},s_1,0,0,0)$
Cm^* (8)[b]	$(0,p_1,p_2)$	$(\bar{\eta},\bar{\eta},s_1,s_2,0,0)$
Pm (6)	$(p_1,0,p_2)$	$(\bar{\eta},\bar{\eta},s_1,0,s_2,0)$
$P1$ (1)	(p_1,p_2,p_3)	$(\bar{\eta},\bar{\eta},s_1,s_2,s_3,0)$

[a]The $Amm2$ phase can also have $P = (p1,0,0)$ with a strain tensor of $(\bar{\eta},\bar{\eta},s_1,0,0,0)$, as seen with $SrSnO_3$ under tension (Fig. S10 in Ref. [45]).

[b]Cm and Cm^* are energetically inequivalent phases with the same space group symmetry.

verified by calculations extending beyond 4% strain (Fig. S11). In a real system, these regions of phase coexistence could be narrower than predicted due to factors not accounted for in this study, such as interface coherency [59].

Of the three systems predicted to display phase coexistence, $PbTiO_3$ displays the largest driving force for this effect to take place. This could be due to the unique bonding characteristics of this system. Previous electronic structure calculations have outlined the pronounced covalency between Pb and O due to the hybridization of the Pb 6s electronic states with the O 2p states [60]. This is contrasted with a system such as $BaTiO_3$, in which the A cation acts as a spherical, nearly completely ionized Ba^{2+} ion. The resulting effect for $PbTiO_3$ is a stronger energetic dependence on atomic displacements, larger ferroelectric distortions, and increased sensitivity of the energy to nonhydrostatic strains [60]. The effect of strain-induced phase coexistence in $PbTiO_3$ is potentially useful for device applications, as has been discussed in recent experimental and computational work [59,61].

Interestingly, the three systems displaying phase coexistence feature soft biaxial elastic responses (i.e., increases in strain energy with increasing misfit strain magnitude) compared to the other (100)-oriented films, as can be appreciated from a comparison of the associated calculated energy curves. This could have important consequences for practical applications, as the lower strain energies, for a given misfit strain, should lead to larger values for the critical thickness for misfit-dislocation formation.

B. (110)-oriented systems

Table III summarizes the different (110)-oriented phases observed in the present calculations, along with their space group symmetries and a description of the polarization and homogeneous strain state (relative to a cubic reference structure). Unlike the situation for (100)-oriented films, the authors are unaware of a standard nomenclature for the different phases that can be derived from the perovskite structure for (110)- and (111)-oriented films, and, in what follows, these are referred to by their space group symbols.

Figure 5(a) plots the polarization and energy versus misfit strain for $BaTiO_3$ with the (110)-growth orientation. The polarization behavior for (110)-oriented $BaTiO_3$ is predicted to be significantly different from the (100)-oriented case. Under large compression, a broad region of the $Amm2$ phase is observed, with a polarization that is oriented out of plane and nearly constant in magnitude versus strain. At small compressive strain, a nonzero P_y component develops and a transition to the Cm^* phase occurs. Finally, at around $\bar{\eta} = 0.4\%$, there is a sudden disappearance of out-of-plane polarization paired with a jump in P_x, signifying a first-order transition to a distinct Cm phase. (110)-oriented $BaTiO_3$ has been studied in Ref. [31], using a first-principles effective Hamiltonian approach with Monte Carlo simulations. The present work predicts the same order of phases versus strain as found in Ref. [31] at the lowest temperature considered (5 K), although the exact values of the strains where the phase transitions occur show slight differences, presumably because of the different computational approaches employed. Three other systems, $KNbO_3$ (Fig. S6), $PbSnO_3$ (Fig. S8), and $NaVO_3$ (Fig. S8), have the same phase sequences and very similar qualitative behavior as $BaTiO_3$. In the case of $NaVO_3$, a $P1$ phase appears at very large tensile misfit strains, with the out-of-plane polarization re-emerging. $NaVO_3$ furthermore has the largest average polarization at nearly 1 C/m^2.

Figure 5(b) gives the polarization and energy dependence on misfit strain for $SrTiO_3$ with the (110)-growth orientation. The qualitative polarization behavior is similar to that for the (100)-oriented case, with a paraelectric region ($Cmmm$ phase) surrounded by phases with out-of-plane polarization under compression ($Amm2$) and in-plane polarization under tension ($Cmm2$–Cm). However, the width of this paraelectric region is larger for (110)-oriented $SrTiO_3$ and is shifted toward more compressive strains compared to the (100)-oriented case. Five other systems exhibit qualitative behavior similar to that illustrated in Fig. 5(b) for $SrTiO_3$, including $KTaO_3$ (Fig. S6), $BaZrO_3$ (Fig. S5), $SrSnO_3$ (Fig. S10), $BaHfO_3$ (Fig. S4), and $BaSnO_3$ (Fig. S4). In the (110)-oriented case, both $BaSnO_3$ and $BaHfO_3$ have paraelectric $Cmmm$ phase regions that extend across the entire range considered.

Figure 5(c) shows the polarization and energetic behavior of $SrHfO_3$ with the (110)-growth orientation. The general behavior is similar to (100)-oriented $SrHfO_3$ shown in Fig. 4(c), both having a first-order transition at 0.2% misfit strain that takes the system from primarily out-of-plane polarization to primarily in-plane polarization. For (110)-oriented $SrHfO_3$, the predicted phase sequence is Pm, with nonzero P_x and P_z polarization components, to $Amm2$, with exclusively nonzero P_z, back to Pm, and finally to $Cmm2$, with exclusively nonzero P_y. $NaTaO_3$ (Fig. S7) has a very similar polarization behavior, with slightly higher polarization magnitudes and an additional intermediate $P1$ phase.

Figure 5(d) shows the polarization and energetic behavior of $PbTiO_3$ with the (110)-growth orientation. A comparison of the results with those for the (100) orientation in Fig. 4(d) illustrates the pronounced effect that film orientation can have on the polarization and energetic behavior. Unlike (100)-oriented $PbTiO_3$, strain-induced phase separation is not

TABLE IV. Summary of the observed (111) epitaxial phases, including the space group, polarization vector, and strain tensor given in Voigt notation. Strains are relative to a cubic $Pm\bar{3}m$ reference structure. p_i and s_i are arbitrary nonzero constants, while $\bar{\eta}$ is misfit strain. The polarization vector and strain tensor components correspond to the coordinate system shown in Fig. 2(c).

Space group	(P_x, P_y, P_z)	$(\epsilon_{xx}, \epsilon_{yy}, \epsilon_{zz}, \epsilon_{yz}, \epsilon_{xz}, \epsilon_{xy})$
$R\bar{3}m$ (166)	(0,0,0)	$(\bar{\eta}, \bar{\eta}, s_1, 0, 0, 0)$
$R3$ (146)	$(0, 0, p_1)$	$(\bar{\eta}, \bar{\eta}, s_1, 0, 0, 0)$
$R3m$ (160)	$(0, 0, p_1)$	$(\bar{\eta}, \bar{\eta}, s_1, 0, 0, 0)$
Cm (8)	$(p_1, 0, p_2)$	$(\bar{\eta}, \bar{\eta}, s_1, 0, s_2, 0)$
Cm (8)[a]	$(p_1, \sqrt{3}p_1, p_2)$	$(\bar{\eta}, \bar{\eta}, s_1, \sqrt{3}s_2, s_2, 0)$
$P1$ (1)	(p_1, p_2, p_3)	$(\bar{\eta}, \bar{\eta}, s_1, s_2, s_3, 0)$

[a]The two Cm phases are equivalent and correspond to a 60° in-plane rotation of the cell.

predicted in any strain regime for the (110) orientation. Instead, four phases appear in roughly evenly spaced strain regimes, with a phase ordering of $Amm2{-}Pm{-}P1{-}Cmm2$. The $P1$ to $Cmm2$ phase transition is first order, with a sudden drop in P_x and P_z, which is replaced by the appearance of a P_y component. Furthermore, the average total polarization magnitude is slightly diminished and much more consistent with changing strain as compared to the (100)-oriented case. Overall, the polarization behavior is much more nuanced for the (110) orientation, with all three components of the polarization growing or diminishing in various strain regimes. Finally, the energy versus misfit strain rises more rapidly in the (110)-oriented case compared to the (100)-oriented structure. $NaNbO_3$ (Fig. S7) shows similar polarization behavior to that shown in Fig. 5(d) for $PbTiO_3$, having an $Amm2{-}Pm{-}P1$ phase sequence. The first-order transition from $P1$ to $Cmm2$ seen for $PbTiO_3$ is, for $NaNbO_3$, replaced by an extended $P1$ phase region with smoothly increasing in-plane polarization and smoothly decreasing out-of-plane polarization.

C. (111)-oriented systems

Table IV summarizes the different (111) phases observed in the present calculations, along with their space group symmetries and a description of the polarization and homogeneous strain state (relative to a cubic reference structure). It is interesting to compare the present results with the list of all symmetry-allowed perovskite phases consistent with (111) epitaxy determined in Ref. [33] (see Table I of Ref. [33]). In the present calculations, only a subset of the possible symmetries listed in Ref. [33] are observed. Specifically, the nonpolar phases with $R32$, and $C2/m$ symmetry as well as the polar phase with the $C2$ symmetry are not found to be energetically stable for any of the systems considered in the present work. In Ref. [33], it is argued that the lowest-symmetry $P1$ phase is unlikely to form in (111)-oriented perovskite films, although this phase is observed in the present calculations for the $SrSnO_3$ and $SrTiO_3$ systems over small strain regimes.

It should be noted that the $R3$ phase in Table IV has a space group that is a subgroup of that for the $R3m$ phase; these two phases share the same polarization direction, but additional atomic displacements in the former case break the mirror symmetry in the latter. Also, the two Cm phases listed in Table IV are energetically equivalent and differ only by an in-plane rotation of the cell by 60°. This difference is equivalent to an in-plane rotation of the measurement axes and is not physically significant.

Figure 6(a) plots the polarization and energy versus misfit strain for $BaTiO_3$ with the (111)-growth orientation. Under large compressive misfit strains, the paraelectric $R\bar{3}m$ phase is predicted to be energetically stable. With decreasing compressive strain, this phase undergoes a second-order transition to the $R3m$ phase with polarization directed normal to the epitaxial plane. At $\bar{\eta} = 0.2\%$, the $R3m$ phase undergoes a first-order transition to the Cm phase with mixed P_x and P_z components. Most striking for this system is the anomalous out-of-plane polarization behavior, which is diminished under compression. This behavior has been predicted previously [32,33], although the paraelectric regions in these works occur at smaller compressive strains. This difference in phase boundary position is again likely to be associated with the details of the calculation methods, due to the near energetic degeneracy of the paraelectric $R\bar{3}m$ phase with the $R3m$ phase for less than -1% compressive strains.

No other (111)-oriented systems considered in this work show this anomalous out-of-plane polarization decrease with increasing compressive strains to any significant extent. $KNbO_3$ (Fig. S6), $PbSnO_3$ (Fig. S8), and $NaVO_3$ [Fig. 6(c)] have similar first-order $R3m$ to Cm transitions under tension, but due to the lack of diminishing P_z under compression, these three systems, which have been grouped with $BaTiO_3$ in the (100)- and (110)-oriented cases, are separately discussed below with $NaVO_3$ as the representative system [Fig. 6(c)]. The unique behavior of $BaTiO_3$ can be explained in terms of elastic arguments. At -4% misfit strain, the out-of-plane tensile strains of $BaTiO_3$, $KNbO_3$, $PbSnO_3$, and $NaVO_3$ are 2.5%, 3.8%, 5.0%, and 6.2%, respectively, showing that $BaTiO_3$ has a significantly smaller out-of-plane strain than the other three systems. This Poisson expansion for (111)-oriented $BaTiO_3$ is much smaller than for the (100)- and (110)-growth orientations. It is suggested in Ref. [32] that the anomalous paraelectric transition of $BaTiO_3$ is the result of compression forcing the oxygen spacing to contract the hollow space above and below the Ti cation, pushing this atom back to its central position. This description, however, does not generalize to the other three similar systems in this work because they are able to significantly expand in the out-of-plane direction, thereby creating space for the B cation to remain off center.

Figure 6(b) shows the polarization and energetic behavior of $SrTiO_3$ with the (111)-growth orientation. From large compressive until modest tensile strain, the $R\bar{3}m$ paraelectric phase is stable. From 0.7% to 1.2% misfit strain, a small region of $P1$ phase is stable, followed by a transition to Cm. Both of these $SrTiO_3$ polar phases have predominantly in-plane polarization. As was the case for the (100) and (110) orientations, five other systems exhibit qualitative behavior similar to that illustrated in Fig. 6(b) for $SrTiO_3$, including $KTaO_3$ (Fig. S6), $BaZrO_3$ (Fig. S5), $SrSnO_3$ (Fig. S10), $BaHfO_3$ (Fig. S4), and $BaSnO_3$ (Fig. S4). In the (111)-oriented case, $BaSnO_3$, $BaZrO_3$, and $BaHfO_3$ all have paraelectric $R\bar{3}m$ phase regions that extend across the entire misfit strain range considered. This polarization behavior group is similar to the paraelectric group in the (100)- and (110)-oriented

cases, except with the absence of a phase with predominantly out-of-plane polarization, even under very large compression.

Figure 6(c) shows the polarization and energetic behavior of $NaVO_3$ with the (111)-growth orientation. This system has a very large and consistent polarization magnitude of around 1 C/m^2 in all strain regimes. Under compression, the $R3m$ phase with large out-of-plane polarization is predicted, while the Cm phase with mixed polarization contributions is predicted under tension. A first-order phase transition between $R3m$ and Cm occurs at just over 1% misfit strain (3.71 Å) and coincides with the point of lowest predicted elastic energy. Given the relative stability and large, sudden change in polarization at this point, moderately tensile-strained $NaVO_3$ could provide interesting properties for device applications. Furthermore, the region of stability is predicted to be broad, showing less than 25 meV metastability relative to the fully relaxed bulk phase throughout −1% to 3% misfit strain (3.64–3.79 Å). This stability is, in part, due to the pronounced asymmetry of the energy curve. For $NaVO_3$, the maximum metastability under 4% compression is over 250 meV, while the maximum under 4% tension is only 50 meV. Two other systems, $KNbO_3$ (Fig. S6) and $PbSnO_3$ (Fig. S8), show similar polarization behavior as $NaVO_3$, both having smaller average polarization magnitudes. Note that the Cm phases are the same for these three systems, as discussed above. These three systems follow the same phase transition sequence as $BaTiO_3$ [Fig. 6(a)], but have been separately grouped due to their nearly constant (and nonvanishing) out-of-plane polarizations under compression.

Figure 6(d) gives the polarization and energy dependence on misfit strain for $PbTiO_3$ with the (111)-growth orientation. Compared to the (100)- [Fig. 4(d)] and (110)-oriented [Fig. 5(d)] cases, (111)-oriented $PbTiO_3$ shows very broad phase regions connected by smooth, second-order transitions and a slightly diminished average polarization magnitude. This system exhibits a single second-order phase transition between an $R3m$ phase having all out-of-plane polarization, and a Cm phase having an additional in-plane polarization component. With increasing tension in the Cm phase, the out-of-plane polarization gradually gives way to predominantly in-plane polarization. As for the (100)- and (110)-oriented cases, $NaNbO_3$ (Fig. S7) shows polarization behavior very similar to $PbTiO_3$ for the (111)-growth orientation. Two additional systems, $SrHfO_3$ (Fig. S9) and $NaTaO_3$ (Fig. S7), display the same qualitative behavior. $NaNbO_3$, $SrHfO_3$, and $NaTaO_3$ have additional $R3{-}R3m$ phase transitions under large compression, which have no effect on the polarization direction (see $R3$ symmetry discussion above). It is interesting to note that $SrHfO_3$ (Fig. S9) and $NaTaO_3$ (Fig. S7), comprising a distinct polarization behavior group in the (100)- and (110)-oriented cases, show behavior similar to $PbTiO_3$ and $NaNbO_3$ under the (111)-growth orientation.

D. Analysis of polarization behaviors

There exists a small number of distinct energetic and polarization behaviors by which compositions considered in this work can be categorized. Six of the 14 systems considered exhibit nonpolar phases over significant ranges of misfit strain. Another four systems, $BaTiO_3$, $KNbO_3$, $PbSnO_3$, and $NaVO_3$, have very similar phase orderings and polarization behaviors in all three orientations. The remaining four systems, $SrHfO_3$, $NaTaO_3$, $PbTiO_3$, and $NaNbO_3$, only loosely group together, having a more diverse set of behaviors and less consistency in their internal groupings across the three orientations. These behavioral groups can be visualized in Figs. S1–S3 of the Supplemental Material [45].

These groupings can be partially explained from geometric considerations. From this perspective, a polar distortion develops to optimize bond lengths, as determined by ionic radii. The Goldschmidt tolerance factor (t) characterizes the propensity of a given perovskite chemistry to distort. Values near unity favor cubic, nonpolar structures, while values far from unity favor distortions. Given the five-atom restriction of the model considered in this work, these distortions must always be polar. The six compositions (tolerance factors) for the behavior group having large nonpolar phase regions are $SrTiO_3$ ($t = 1.001$), $KTaO_3$ (1.085), $BaZrO_3$ (1.000), $SrSnO_3$ (0.957), $BaHfO_3$ (1.007), and $BaSnO_3$ (1.016). Four of the six systems have tolerance factors very near unity. However, it is unusual that $KTaO_3$ and $SrSnO_3$ should maintain any regions of paraelectricity given the ratios of their ionic radii. Furthermore, it is unclear why $BaSnO_3$ does not undergo a polar distortion under any amount of misfit strain given that its tolerance factor deviates from unity by a non-negligible amount. The four compositions (tolerance factors) composing the second behavior group are $BaTiO_3$ ($t = 1.063$), $KNbO_3$ (1.090), $PbSnO_3$ (0.955), and $NaVO_3$ (1.028). Three of the four systems have B cations that are relatively too small in the cubic perovskite structure, while $PbSnO_3$ is seemingly anomalous, having an A cation that is too large and is thus expected to have differing polarization behavior from the other three. The final group of compositions (tolerance factors) are $SrHfO_3$ ($t = 0.949$), $NaTaO_3$ (0.968), $PbTiO_3$ (0.999), and $NaNbO_3$ (0.972). The seemingly anomalous system in this case is $PbTiO_3$, which, based on ionic radii, should group with the six nonpolar compositions. To reconcile the exceptional systems, we consider additional features of the bonding.

From an electronic standpoint, ferroelectricity is not favored in a perovskite system that features purely ionic bonding. Rather, polar distortions are understood to be stabilized by the development of covalent character in the bonding of one or more cations with oxygen [62]. Two ways in which this mixed ionic-covalent bonding appears are through lone-pair s electronic states on the A cation (e.g., Pb^{2+}) as well as energetically low-lying empty d orbitals on the B cation (e.g., Ti^{4+}, Nb^{5+}). In both cases, these electronic states hybridize with occupied oxygen $2p$ orbitals to stabilize a polar distortion [63]. These considerations help explain some of the anomalies described above. For example, $SrSnO_3$ and $BaSnO_3$ have A cations that lack lone-pair electrons and B cations that lack empty d orbitals. These two systems are expected to exhibit more ionic character in their bonding, which in turn could explain the tendency of these two systems to remain nonpolar over a larger misfit strain regime than expected. Furthermore, $PbSnO_3$ has an A cation with lone-pair electrons but a B cation lacking empty d orbitals. Thus, for this system, the A cation is expected to feature enhanced covalent character in its bonding with oxygen, while the B cation will be primarily ionic. This is the reverse of the behavior of the other three

systems sharing a behavior group with $PbSnO_3$. Under these circumstances, it is possible that a system with tolerance factor less than one can behave similarly to those with tolerance factors greater than one if the electronic character of the cation species is swapped. Finally, $PbTiO_3$ ($t = 0.999$) is highly susceptible to covalency, having both *A* and *B* cations capable of hybridizing with oxygen. This could possibly explain why a nonpolar phase is never predicted, despite this system's geometric amenity to a nonpolar structure. The qualitative considerations above serve to highlight the geometrical and bonding factors that underlie the main trends in the computed results. However, more work is required to develop quantitative theories for the strain dependencies of polarization. This is highlighted by the case of $KTaO_3$. Based on geometric and electronic considerations, this system should behave most similarly to systems in the $BaTiO_3$ group, but instead $KTaO_3$ exhibits a nonpolar phase over a large range of misfit strain.

IV. SUMMARY

The effects of epitaxial misfit strain on the structure, polarization, and energetic behavior of 42 nonmagnetic perovskite thin-film systems have been investigated using an automated first-principles computational approach. These 42 systems are comprised of 14 compositions modeled for the (100)-, (110)-, and (111)-growth orientations. The results indicate robust trends of in-plane polarization enhancement under tension for all growth orientations and out-of-plane polarization enhancement with compression for the (100)- and (110)-oriented systems. For the (111)-growth orientation, a wider variety of out-of-plane polarization behaviors is seen, with $BaTiO_3$ exhibiting an anomalously diminishing out-of-plane polarization with compression.

The computational results further reveal a clear tendency for compounds with different compositions to form behavior groups, characterized by their phase sequences and polarizations versus misfit strain. Two (100)-oriented systems, $SrHfO_3$ and $NaTaO_3$, exhibit unique polarization dependencies on misfit strain, having phase transitions near 0% misfit strain whereby a phase with all out-of-plane polarization gives way to a phase with all in-plane polarization. The three (100)-oriented systems showing strain-induced phase coexistence, $PbTiO_3$, $NaNbO_3$, and $NaVO_3$, have relatively soft biaxial elastic responses compared to the other compounds where this phenomenon is absent. This suggests that softness of the in-plane biaxial elastic response is an important factor in predicting whether or not strain-induced phase coexistence will occur in a film.

This work demonstrates the profound effect of growth orientation on the polarization behavior of thin films. For example, the smooth, second-order phase transitions and strain-induced phase coexistence exhibited by (100)-oriented $PbTiO_3$ are replaced by a complex interplay of the three polarization components and a first-order transition in (110)-oriented $PbTiO_3$. While most of the other compounds show similar sensitivity to growth orientation, the six compositions, $SrTiO_3$, $KTaO_3$, $BaZrO_3$, $SrSnO_3$, $BaHfO_3$, and $BaSnO_3$, show similar paraelectric behavior between the (100), (110), and (111) orientations. Further, the (110)- and (111)-oriented films more commonly feature first-order phase transitions as a function of misfit strain, relative to the (100) case. An example is (111)-oriented $NaVO_3$, having a first-order phase transition at small tensile strains with a very large shift in polarization direction. As sudden changes in polarization state are often useful for device applications, the relatively unexplored realm of (110)- and (111)-oriented films could provide a fruitful domain for materials discovery.

ACKNOWLEDGMENTS

This work was intellectually led by the Department of Energy (DOE) Basic Energy Sciences (BES) program, the Materials Project, under Grant No. EDCBEE. T.A. acknowledges support from a National Science Foundation Graduate Research Fellowship (Grant No. DGE1106400). L.W.M. acknowledges support of the National Science Foundation under Grant No. CMMI-1434147. This research used resources of the National Energy Research Scientific Computing Center, a DOE Office of Science User Facility supported by the Office of Science of the U.S. Department of Energy under Contract No. DE-AC02-05CH11231.

[1] J. F. Scott, Science **315**, 954 (2007).
[2] L. E. Cross and R. E. Newnham, in *Ceramics and Civilization* (American Ceramic Society, Westerville, OH, 1987), Vol. III, pp. 289–305.
[3] B. Jaffe, W. R. Cook, and H. L. Jaffe, *Piezoelectric Ceramics* (Academic Press, New York, 1971).
[4] A. R. Damodaran, J. C. Agar, S. Pandya, Z. Chen, L. Dedon, R. Xu, B. Apgar, S. Saremi, and L. W. Martin, J. Phys.: Condens. Matter **28**, 263001 (2016).
[5] D. G. Schlom, L. Q. Chen, C. B. Eom, K. M. Rabe, S. K. Streiffer, and J. M. Triscone, Annu. Rev. Mater. Res. **37**, 589 (2007).
[6] L. W. Martin, Y. H. Chu, and R. Ramesh, Mater. Sci. Eng. **68**, 89 (2010).
[7] J. H. Haeni, P. Irvin, W. Chang, R. Uecker, P. Reiche, Y. L. Li, S. Choudhury, W. Tian, M. E. Hawley, B. Craigo, A. K. Tagantsev, X. Q. Pan, S. K. Streiffer, L. Q. Chen, S. W. Kirchoefer, J. Levy, and D. G. Schlom, Nature (London) **430**, 758 (2004).
[8] D. G. Schlom, L. Q. Chen, X. Pan, A. Schmehl, and M. A. Zurbuchen, J. Am. Ceram. Soc. **91**, 2429 (2008).
[9] K. Sone, H. Naganuma, T. Miyazaki, T. Nakajima, and S. Okamura, Jpn. J. Appl. Phys. **49**, 09MB03 (2010).
[10] R. Xu, S. Liu, I. Grinberg, J. Karthik, A. R. Damodaran, A. M. Rappe, and L. W. Martin, Nat. Mater. **14**, 79 (2015).
[11] W. K. Simon, E. K. Akdogan, and A. Safari, J. Appl. Phys. **97**, 103530 (2005).
[12] A. K. Tagantsev, N. A. Pertsev, P. Muralt, and N. Setter, Phys. Rev. B **65**, 012104 (2001).
[13] H. Wu, X. Ma, Z. Zhang, J. Zeng, J. Wang, and G. Chai, AIP Adv. **6**, 015309 (2016).

[14] J. C. Agar, S. Pandya, R. Xu, A. K. Yadav, Z. Liu, T. Angsten, S. Saremi, M. Asta, R. Ramesh, and L. W. Martin, MRS Commun. **6**, 151 (2016).
[15] M. Dawber, K. M. Rabe, and J. F. Scott, Rev. Mod. Phys. **77**, 1083 (2005).
[16] J. Schwarzkopf and R. Fornari, Prog. Cryst. Growth Charact. Mater. **52**, 159 (2006).
[17] H. Béa, B. Dupé, S. Fusil, R. Mattana, E. Jacquet, B. Warot-Fonrose, F. Wilhelm, A. Rogalev, S. Petit, V. Cros, A. Anane, F. Petroff, K. Bouzehouane, G. Geneste, B. Dkhil, S. Lisenkov, I. Ponomareva, L. Bellaiche, M. Bibes, and A. Barthélémy, Phys. Rev. Lett. **102**, 217603 (2009).
[18] S. Curtarolo, G. L. W. Hart, M. B. Nardelli, N. Mingo, S. Sanvito, and O. Levy, Nat. Mater. **12**, 191 (2013).
[19] G. Ceder and K. Persson, Sci. Am. **309**, 36 (2013).
[20] B. Meredig, A. Agrawal, S. Kirklin, J. E. Saal, J. W. Doak, A. Thompson, K. Zhang, A. Choudhary, and C. Wolverton, Phys. Rev. B **89**, 094104 (2014).
[21] A. Jain, G. Hautier, S. P. Ong, and K. Persson, J. Mater. Res. **31**, 977 (2016).
[22] A. Zakutayev, X. Zhang, A. Nagaraja, L. Yu, S. Lany, T. O. Mason, D. S. Ginley, and A. Zunger, J. Am. Chem. Soc. **135**, 10048 (2013).
[23] R. Resta and D. Vanderbilt, Top. Appl. Phys. **105**, 31 (2007).
[24] R. D. King-Smith and D. Vanderbilt, Phys. Rev. B **49**, 5828 (1994).
[25] J. B. Neaton, C. L. Hsueh, and K. M. Rabe, *Materials Research Society Symposium: Proceedings* (MRS, Warrendale, PA, 2002), Vol. 718.
[26] O. Diéguez, S. Tinte, A. Antons, C. Bungaro, J. B. Neaton, K. M. Rabe, and D. Vanderbilt, Phys. Rev. B **69**, 212101 (2004).
[27] A. Antons, J. B. Neaton, K. M. Rabe, and D. Vanderbilt, Phys. Rev. B **71**, 024102 (2005).
[28] K. M. Rabe, Curr. Opin. Solid State Mater. Sci. **9**, 122 (2005).
[29] O. Diéguez, K. M. Rabe, and D. Vanderbilt, Phys. Rev. B **72**, 144101 (2005).
[30] O. Diéguez and D. Vanderbilt, Phase Transit. **81**, 607 (2008).
[31] Z. Gui, S. Prosandeev, and L. Bellaiche, Phys. Rev. B **84**, 214112 (2011).
[32] A. Raeliarijaona and H. Fu, J. Appl. Phys. **115**, 054105 (2014).
[33] R. Oja, K. Johnston, J. Frantti, and R. M. Nieminen, Phys. Rev. B **78**, 094102 (2008).
[34] N. A. Benedek and C. J. Fennie, J. Phys. Chem. C **117**, 13339 (2013).
[35] A. Togo and I. Tanaka, Scr. Mater. **108**, 1 (2015).
[36] J. Hutter, Wiley Interdiscip. Rev.: Comput. Mol. Sci. **2**, 604 (2012).
[37] C. J. Pickard and R. J. Needs, J. Phys.: Condens. Matter **23**, 053201 (2011).
[38] C. W. Glass, A. R. Oganov, and N. Hansen, Comput. Phys. Commun. **175**, 713 (2006).
[39] Y. Wang, J. Lv, L. Zhu, and Y. Ma, Comput. Phys. Commun. **183**, 2063 (2012).
[40] K. Momma and F. Izumi, J. Appl. Crystallogr. **44**, 1272 (2011).
[41] V. M. Goldschmidt, Naturwissenschaften **14**, 477 (1926).
[42] I. D. Brown, Chem. Soc. Rev. **7**, 359 (1978).
[43] www.me.utexas.edu/˜benedekgroup/ToleranceFactorCalculator
[44] K. M. Rabe, M. Dawber, C. Lichtensteiger, C. H. Ahn, and J. M. Triscone, Top. Appl. Phys. **105**, 1 (2007).
[45] See Supplemental Material at http://link.aps.org/supplemental/10.1103/PhysRevB.95.174110 for additional details regarding the automated workflow used to generate energetic and polarization data. Additional figures also provide a look at all of the data produced in this work. Figures S1–S3 depict the polarization behavior groupings for each of the three growth orientations, and Figs. S4–S11 plot the energies and polarizations versus misfit strain for all systems considered in this work.
[46] G. Kresse and J. Hafner, Phys. Rev. B **47**, 558 (1993).
[47] G. Kresse and J. Hafner, Phys. Rev. B **49**, 14251 (1994).
[48] G. Kresse and J. Furthmüller, Phys. Rev. B **54**, 11169 (1996).
[49] G. Kresse and J. Furthmüller, Comput. Mater. Sci. **6**, 15 (1996).
[50] J. P. Perdew and A. Zunger, Phys. Rev. B **23**, 5048 (1981).
[51] P. E. Blöchl, Phys. Rev. B **50**, 17953 (1994).
[52] G. Kresse and D. Joubert, Phys. Rev. B **59**, 1758 (1999).
[53] H. Monkhorst and J. Pack, Phys. Rev. B **13**, 5188 (1976).
[54] A. M. Kolpak, N. Sai, and A. M. Rappe, Phys. Rev. B **74**, 054112 (2006).
[55] K. M. Indlekofer and H. Kohlstedt, Europhys. Lett. **72**, 282 (2005).
[56] D. I. Bilc, R. Orlando, R. Shaltaf, G. M. Rignanese, J. Íñiguez, and P. Ghosez, Phys. Rev. B **77**, 165107 (2008).
[57] T. Schimizu and T. Kawakubo, Jpn. J. Appl. Phys. **37**, L235 (1998).
[58] N. A. Pertsev, A. G. Zembilgotov, and A. K. Tagantsev, Phys. Rev. Lett. **80**, 1988 (1998).
[59] F. Xue, Y. Li, Y. Gu, J. Zhang, and L. Q. Chen, Phys. Rev. B **94**, 220101 (2016).
[60] R. Cohen and H. Krakauer, Ferroelectrics **136**, 65 (1992).
[61] A. R. Damodaran and L. W. Martin (unpublished).
[62] N. A. Spaldin, in *Analogies and Differencies between Ferroelectrics and Ferromagnets*, edited by K. M. Rabe, C. H. Ahn, and J. M. Triscone, Physics of Ferroelectrics (Springer-Verlag, Berlin, 2007), pp. 175–217.
[63] W. Zhong, D. Vanderbilt, R. D. King-Smith, and K. Rabe, Ferroelectrics **164**, 291 (1995).